Structure and Tracer Kinetics-Driven Dynamic PET Reconstruction

Jianan Cui[®], Zhongya Qin, Shuhang Chen, Yunmei Chen, and Huafeng Liu[®], Member, IEEE

Abstract—Dynamic positron emission tomography (dPET) is a nuclear medical imaging technology that shows the changes in radioactivity over time. In this article, we propose a structure and tracer kinetics-constrained reconstruction framework for dPET imaging. Given the Poisson nature of PET imaging, we integrate the sparse penalty on a dual dictionary into a Poisson-likelihood estimator. Explicit anatomical constraints with a structural dictionary constructed from magnetic resonance or computed tomography images are employed to take advantage of the anatomical imaging modalities. In the kinetic dictionary, we treat tracer kinetics as random variables in a physiologically plausible range based on a compartmental model. We demonstrate the performance of our proposed framework with a direct simulated data set and real patient data.

Index Terms—Compartmental model, dictionary learning and sparse representation, dynamic PET (dPET) image reconstruction.

I. INTRODUCTION

THROUGH scanning for a period of time, dynamic positron emission tomography (dPET) imaging acquires data in a series of frames. The reconstructed images of dPET can show the changes in radioactivity over time. This is useful in oncology, where there is a need to identify the characteristics of cancer, which might go undetected using conventional static PET imaging [1]–[3]. Numerous studies have shown that dPET is a powerful tool for detecting the alterations in glucose metabolism to diagnose cardiovascular diseases [4], [5] as well as myocardial blood-flow analysis [6]. In neurology, dPET is helpful for the study of Alzheimer disease [7] and epilepsy [8]. The main challenge of dPET is the tradeoff between spatial and temporal resolution. To maintain a high-temporal resolution to capture the variation in the tissue, we especially need to

Manuscript received February 15, 2018; revised September 20, 2018, March 14, 2019, and July 20, 2019; accepted October 10, 2019. Date of publication October 16, 2019; date of current version July 2, 2020. This work was supported in part by the National Natural Science Foundation of China under Grant U1809204, Grant 61525106, Grant 61427807, and Grant 61701436, in part by the National Key Technology Research and Development Program of China under Grant 2017YFE0104000 and Grant 2016YFC1300302, and in part by the Shenzhen Innovation Funding under Grant JCYJ20170818164343304 and Grant JCYJ20170816172431715. The work of S. Chen and Y. Chen was supported in part under Grant NSF DMS1719932. (Corresponding author: Huafeng Liu.)

- J. Cui, Z. Qin, and H. Liu are with the State Key Laboratory of Modern Optical Instrumentation, College of Optical Science and Engineering, Zhejiang University, Hangzhou 310027, China (e-mail: liuhf@zju.edu.cn).
- S. Chen and Y. Chen are with the Department of Mathematics, University of Florida, Gainesville, FL 32611 USA.

Color versions of one or more of the figures in this article are available online at http://ieeexplore.ieee.org.

Digital Object Identifier 10.1109/TRPMS.2019.2947860

limit the photon counts in each frame of dPET images, which may lead to very noisy images [9], [10].

AS PET imaging reconstruction is an ill-posed problem, introducing additional penalty constraints is a well-appreciated approach [11]. Many penalty constraints have been adapted to assist with the reconstruction, including the use of quadratic smoothness [12], log-cosh penalization [13], generalized Gaussian [14], Huber potential function [15], Gibbs distribution [16], total variation [17], nonlocal mean [18], temporal basis functions [19], and deep neural network-based prior [20], [21]. In recent studies, advances in hybrid imaging have made the use of anatomical images from computed tomography (CT) and magnetic resonance imaging (MRI) [22] possible. In [23], a modified regularizer, which accounts for the anatomical boundary side information, was introduced into a penalized-likelihood single-photon emission CT (SPECT) reconstruction method to achieve accurate estimates of the activity distribution. Chen et al. [24] tried to utilize a structural dictionary, trained from CT images, to provide intrinsic anatomical structures when they reconstructed the PET images. Chen et al. [25] showed the effectiveness of reconstructing different MR images under the same acquisition sequence via sparse representation by a dictionary trained from the same sequence.

Considering kinetics-based priors can provide physiological and pathophysiological information about the metabolism of substances in a biological system [26], some research efforts have attempted to incorporate a kinetic model that can quantify the underlying physiological processes to help in the dPET reconstruction [27], [28]. Verhaeghe *et al.* [29] introduced exponential-spline wavelets (E-spline wavelets) as base functions for dPET reconstruction. The E-spline wavelets naturally arise from the compartmental description of the dynamics of the tracer distribution [29]. Tong and Shi [30] described a method that formulates the dPET reconstruction in a state-space representation, where a compartmental model serves as a continuous-time system equation to describe the tracer kinetic processes.

Recently, with the development of PET-MR and PET-CT scanners, more accurate co-registration images and functional data could be acquired and made it possible to combine both anatomical and kinetic constraints together into dPET reconstruction, which might further improve the quality of dPET image. Tang *et al.* [31] proposed a direct kinetic parameter reconstruction method in which a co-registered MR image provided prior information by a joint entropy penalty. Novosad and Reader [32] developed a highly constrained

2469-7311 © 2019 IEEE. Personal use is permitted, but republication/redistribution requires IEEE permission. See https://www.ieee.org/publications/rights/index.html for more information.

dPET reconstruction method using both spectral analysis temporal basis functions and spatial basis functions derived from the kernel method applied to a co-registered T1-weighted MR image. Gong *et al.* [33] added MRI information into a Patlak reconstruction model based on the kernel method.

In this article, we describe a tracer kinetics-constrained framework for dynamic reconstruction from the sequences of acquired sinograms with the aid of structural constraints. Our efforts are different from the previous reconstruction studies in two aspects. First, instead of making ad hoc mathematical assumptions, we construct a kinetic dictionary in which the parameters of the tracer kinetics are treated as random variables within a physiologically plausible range based on the general compartmental model. Second, we do have explicit anatomical constraints with a structural dictionary constructed from MR or CT images to take advantage of the strengths of anatomical imaging modalities. Given the Poisson nature of PET measurements, we integrate the sparse penalty on a dual dictionary (DD) into a Poisson-likelihood estimator in which an efficient expectation-maximization (EM) method is used to solve the optimization problem.

The main contributions of this article include: 1) combining the kinetic dictionary and structure dictionary together to constrain PET image reconstruction and 2) using the general tracer compartmental model to construct the kinetic dictionary. Traditional direct reconstruction methods [33]–[36] require the accurate kinetic models to be known, which may be violated in patient data given spatial heterogeneity. The proposed method (essentially indirect reconstruction) uses tracer kinetics as a soft constraint and may be more flexible to handle model mismatch.

II. Метнор

We treat the images of the activity maps as state variables and estimate them from dynamic data by using a robust iterative algorithm. The framework consists of five components: 1) a dPET imaging model; 2) a spatial sparsity constraint via a structural dictionary containing anatomical information; 3) a temporal sparsity constraint via a kinetic dictionary derived from the compartmental model; 4) a formulation of the reconstruction problem using both kinetic and structural penalty constraints; and 5) a robust iterative solution. Each of the five components is presented in the following sections.

A. PET Data and Imaging Model

By scanning from several detector bins over time, we can get the sequence $Y \in \mathbb{R}^{I \times F}$, which is organized as an array of coincidence events y_{if} collected by all the I detector pairs indexed by $i=1,\ldots,I$ from all the F frames indexed by $f=1,\ldots,F$. The aim of dPET reconstruction is to acquire the set of true activity maps $X \in \mathbb{R}^{J \times F} = \{x_{jf}, j=1,\ldots,J,f=1,\ldots,F\}$, where j is the jth pixel of the total J pixels. The fth frame of the activity maps can be denoted as $X_f \in \mathbb{R}^{J \times 1}$.

Because PET data follow the Poisson distribution, the measured data y_{if} in the fth frame can be described as a collection

of independent Poisson random variables with expectation values \bar{y}_{if} . \bar{y}_{if} are related to the unknown activities x_{jf} through an affine transform

$$y_{\rm if} \sim \text{Poisson}\{\bar{y}_{\rm if}\}$$
 s.t. $\bar{y}_{\rm if} = \sum_{j}^{J} g_{ij}x_{jf} + r_{\rm if} + s_{\rm if}$ (1)

where g_{ij} represents the *ij*th entry of the system matrix $G \in \mathbb{R}^{I \times J}$, and r_{if} and s_{if} are the expectation of random events and scattered events, respectively.

The likelihood function of Y is

$$\Pr(Y|X) = \prod_{f}^{F} \prod_{i}^{I} e^{-\bar{y}_{if}} \frac{\bar{y}_{if}^{y_{if}}}{y_{if}!}.$$
 (2)

To calculate more conveniently, we do not maximize the above likelihood function directly. Instead, we minimize its negative log-likelihood function to estimate X

$$\min_{X} L(X) = \min_{X} -\log \Pr(Y|X)$$

$$= \min_{X} \left(\sum_{f}^{F} \sum_{i}^{I} \bar{y}_{if} - y_{if} \log \bar{y}_{if} \right)$$
s.t. $\bar{y}_{if} = \sum_{i}^{J} g_{ij}x_{jf} + r_{if} + s_{if}$. (3)

In (3), the constant term $log(y_{if}!)$ has been neglected. Because PET reconstruction is an ill-posed problem, penalty terms will be incorporated into this likelihood function to assist in the reconstruction.

B. Spatial Sparse Representation

In this section, we construct a structural dictionary learned from anatomical images with structures similar to those of PET images.

First, a structural dictionary D_S that contains local features from the corresponding images is trained by the K-SVD algorithm [37]. This algorithm achieves this by using an iterative method that alternates between the sparse coding of the anatomical image based on the current dictionary and a process that updates the dictionary atoms to better fit the said image [37]. Then, the learned dictionary (a set of overcomplete bases) is set as the structural dictionary for the proposed method. The inherent redundancy of the structural dictionary will lead to a sparser representation of our reconstructed PET image.

The procedure to drive the structural penalty constraint is described next. Each frame of the PET images to be reconstructed is decomposed into V overlapping patches. The size of a patch is $\sqrt{n} \times \sqrt{n}$, and it can be expressed as an n-dimensional vector. E_v is a matrix operator for extracting the vth patch from the fth frame activity map, $Patch_{vf} = E_v X_f \in \mathbb{R}^n$, v = 1, ..., V. The vth patch from the fth frame can be sparsely represented by the elements of the learned structural dictionary $D_S \in \mathbb{R}^{n \times Z}$ as $Patch_{vf} = D_S \alpha_{vf}$. Here, Z is the number of atoms in the dictionary to be trained and the variate $\alpha_{vf} \in \mathbb{R}^{Z \times 1}$ is the sparse coefficient of $Patch_{vf}$ [37]. Therefore,

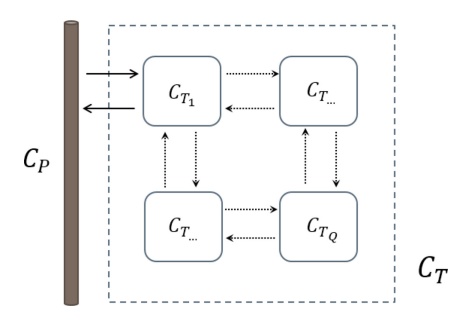


Fig. 1. General tracer compartmental model. There are $\mathcal Q$ tissue compartments in this model.

the sparsity of X_f under the representation of D_S can be introduced as a regularization in the reconstruction. The structural sparse penalty is as follows:

$$S_S(X,\alpha) = \sum_{f}^{F} \sum_{\nu}^{V} \|E_{\nu}X_f - D_S\alpha_{\nu f}\|_{2}^{2} + \mu_S\|\alpha_{\nu f}\|_{1}$$
 (4)

where $\alpha = \{\alpha_{vf}, v = 1, \dots, V, f = 1, \dots, F\}$, μ_S is a weighting parameter, and $\|\cdot\|_1$ is the l_1 -norm. The first term in (4) means that the vth patch from the fth frame image can be represented by a linear combination of the learned structure dictionary D_S through the coefficient α_{vf} . The second term in (4) indicates that the coefficient α_{vf} must be sparse.

C. Tracer Kinetics Prior and Temporal Sparsity

In this section, we will construct a kinetic dictionary D_K from the compartmental model.

The compartmental model is usually adopted to describe the distribution of radiolabeled tracers *in vivo*. A compartment is a mathematical abstraction that represents a particular form or location of a tracer behaving in a kinetically equivalent manner. The interconnections between the compartments are due to the fluxes of material and biochemical conversions [38]. Several groups have introduced compartmental models to help reconstruct PET images [29], [30], [34], [39]. Among these models, the two-compartmental model is the most widely used. However, in this article, we would like to introduce a general tracer compartmental model [40], the structure of which is shown in Fig. 1.

In the general tracer compartmental model (see Fig. 1), C_P represents the arterial tracer concentration in the plasma and C_T is the total tissue radioactivity concentration. There are Q different compartments in this model, and the tracer exchange rates vary between different compartments. According to this general tracer compartmental model, the kinetic process in any voxel is dominated by a set of first-order linear differential equations [40]. The kinetic equations of the above system were solved by Gunn *et al.* [38], [40]. They found an expression for the total tissue radioactivity concentration C_T in terms of a plasma input function

$$C_T(t) = \left[\beta_0 \delta(t) + \sum_{q}^{Q} \beta_q e^{-\theta_q t} \right] \otimes C_I(t)$$
 (5)

where $C_T(t)$ is the total tissue radioactivity concentration at time t. Here, \otimes is the convolution operator, $C_I(t)$ is the concentration of the input function (plasma) at time t, and $\delta(t)$ is an impulse function. In this model, the number of compartments is not set in advance, and, therefore, it is expressed by the parameter q, which represents the qth number of the total number Q of tissue compartments in the target tissue. When $q=1,\ldots,Q$, β_q and θ_q are the coefficients for different compartments, whereas β_0 is the coefficient for the input function.

Equation (5) can be expressed as an expansion in the basis

$$C_T(t) = \sum_{q=0}^{Q} \beta_q \varphi_q \tag{6}$$

where $\varphi_0(t) = C_I(t)$ and $\varphi_q(t) = \int_0^t e^{-\theta_q(t-\tau)} C_I(\tau) d\tau$.

The total tissue radioactivity concentration C_T generates the PET measurements directly through positron emission. Therefore, in dPET imaging, the activity in the fth frame represents the accumulation of the total concentration of radioactivity in the scanning time interval $[t_f^s, t_f^e]$. The value of the jth pixel in the activity map at the fth frame can be expressed by the integral of C_T^j as

$$x_{jf} = \int_{t_f^s}^{t_f^e} C_T^j(t) dt \tag{7}$$

where $C_T^j(t)$ is the concentration of the target tissue for the jth pixel, whereas t_f^s and t_f^e are the start and end scan times, respectively, of the fth frame.

Then, combining (6) and (7), we can represent the entire activity maps as

$$X^{\top} = D_K \beta \tag{8}$$

where the superscript $^{\top}$ refers to the transpose of the matrix, $\beta \in \mathbb{R}^{(W+1)\times J}$ is a coefficient matrix, and $D_K \in \mathbb{R}^{F\times (W+1)}$ is given by

$$D_{K} = \begin{bmatrix} dk_{01} & \cdots & dk_{w1} & \cdots & dk_{W1} \\ \vdots & \ddots & \vdots & \ddots & \vdots \\ dk_{0f} & \cdots & dk_{wf} & \cdots & dk_{Wf} \\ \vdots & \ddots & \vdots & \ddots & \vdots \\ dk_{0F} & \cdots & dk_{wF} & \cdots & dk_{WF} \end{bmatrix}$$

$$dk_{0f} = \int_{t_{f}^{s}}^{t_{f}^{s}} C_{I}(t)dt$$

$$dk_{wf} = \int_{t_{f}^{s}}^{t_{f}^{s}} \int_{0}^{t} e^{-\theta_{w}(t-\tau)} C_{I}(\tau)d\tau dt. \tag{9}$$

Because the delayed coefficient θ_q in (6) is unknown, and assuming that θ_q is in a physiologically plausible range $[\theta_{\min}, \theta_{\max}]$, we would like to preselect W delayed coefficients in this range as a kinetic spectrum. Here, $\theta_w(w=1,\ldots,W)$ is used to express the wth preselected delayed coefficient. The values of θ_w are spaced logarithmically. We try to obtain a good coverage of the kinetic spectrum by choosing a large enough value for W, which leads to an overcomplete basis (W+1>F) [40]. In the kinetic dictionary D_K , each row

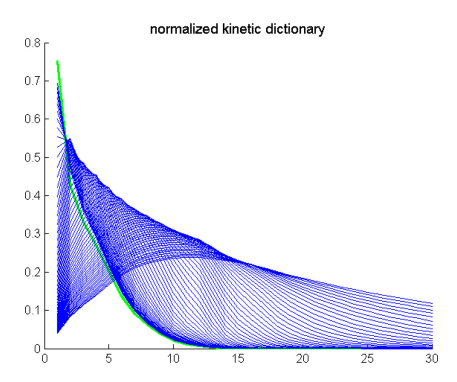


Fig. 2. Normalized kinetic dictionary. The green line shows the plasma input basis with w = 0. The blue lines show the plasma input basis with different values of w.

refers to the kinetic spectrum in a frame. Each column of the dictionary D_K is a function that changes with time, which acts as a basis function of the time-activity curve (TAC). By choosing several functions from the kinetic dictionary D_K and combining them linearly with a suitable coefficient matrix β , as shown in (8), we can fit the TAC of a region of interest (ROI) or a voxel. The normalized kinetic dictionary is shown in Fig. 2.

On the basis of the compartmental model, we can fit the TAC by choosing a few elements in the kinetic dictionary. This idea leads to the following penalty term:

$$S_K(X, \beta) = \|X^\top - D_K \beta\|_2^2 + \mu_K \|\beta\|_1$$
 (10)

where μ_K is a relative weighting parameter for the kinetic sparse constraint.

D. Objective Function

To improve the quality of the reconstructed image, we include information about the structure and tracer kinetics. We try to introduce both structural and kinetic dictionaries to represent the reconstructed dPET images sparsely. For a penalized maximum-likelihood reconstruction algorithm, we estimate the activity maps X by minimizing an objective function consisting of a likelihood function and penalty terms. Thus, the objective function is defined as

$$\min_{X,\alpha,\beta} \Psi(X,\alpha,\beta) = \min_{X,\alpha,\beta} L(X) + p_S S_S(X,\alpha) + p_K S_K(X,\beta) \quad (11)$$

where $S_S(X, \alpha)$ is the structural penalty term in (4) and $S_K(X, \beta)$ is the kinetic penalty term in (10), whereas p_S and p_K are the corresponding weighting parameters. By adjusting the value of the weighting parameters, we can control the contribution of each penalty term.

E. Optimization Technique

We aim to find an optimization algorithm to minimize the objective function (11). Because there are three unknown variables, namely, X, α , and β , we choose a method that calculates one of the variables while the other two are held fixed. The specific algorithm is as follows.

1) X Subproblem: Because the X subproblem is a typical maximum a posterior (MAP) reconstruction problem, we choose an efficient EM-based algorithm to optimize it. When α and β are fixed, the optimization function of the X subproblem is

$$X = \arg\min_{X} \Psi_{X}(X, \alpha, \beta)$$

$$= \arg\min_{X} \sum_{f}^{F} \sum_{i}^{I} \bar{y}_{if} - y_{if} \log \bar{y}_{if}$$

$$+ p_{S} \sum_{f}^{F} \sum_{v}^{V} \|E_{v}X_{f} - D_{S}\alpha_{vf}\|_{2}^{2} + p_{K} \|X^{T} - D_{K}\beta\|_{2}^{2}$$
s.t. $\bar{y}_{if} = \sum_{j}^{J} g_{ij}x_{jf} + r_{if} + s_{if}$. (12)

Following the hidden variable formulation [41], (12) is equivalent to

$$X = \arg\min_{X} \Psi_{X}(c_{ijf}, X, \alpha, \beta)$$

$$= \arg\min_{X} \sum_{f}^{F} \sum_{j}^{J} \sum_{i}^{I} (g_{ij}x_{jf} - c_{ijf} \log(g_{ij}x_{jf}))$$

$$+ p_{S} \sum_{f}^{F} \sum_{v}^{V} \|E_{v}X_{f} - D_{S}\alpha_{vf}\|_{2}^{2} + p_{K} \|X^{\top} - D_{K}\beta\|_{2}^{2}$$
(13)

where a hidden variable c_{ijf} is introduced to (12). It represents the number of photons emitted from image pixel j and detected at the line of response i in the fth frame. Then, the EM algorithm proceeds in two steps.

In the E-step, the hidden variable c_{ijf} is estimated from a conditional expectation $\xi(c_{ijf}|y_{if},x_{jf}^k)$, as shown in (14) [41]. Then, the estimated value \widehat{c}_{ijf} is added to $\Psi_X(c_{ijf},X,\alpha,\beta)$ to obtain a new $\widehat{\Psi}_X(\widehat{c}_{ijf},X,\alpha,\beta)$

$$\widehat{c}_{ijf} = \xi \left(c_{ijf} | y_{if}, x_{jf}^{k} \right) = \frac{g_{ij} x_{jf}^{k}}{\sum_{j}^{J} g_{ij} x_{jf}^{k} + r_{if} + s_{if}} y_{if}$$

$$\widehat{\Psi}_{X} (\widehat{c}_{ijf}, X, \alpha, \beta) = \sum_{f}^{F} \sum_{i}^{J} \sum_{j}^{J} g_{ij} x_{jf} - \widehat{c}_{ijf} \log(g_{ij} x_{jf})$$

$$+ p_{S} \sum_{f}^{F} \sum_{v}^{V} \left\| E_{v} X_{f} - D_{S} \alpha_{vf} \right\|_{2}^{2}$$

$$+ p_{K} \left\| X^{\top} - D_{K} \beta \right\|_{2}^{2}$$

$$(15)$$

where x_{if}^k means the current estimate in the kth iteration.

In the M-step, the intermediate function $\widehat{\Psi}_X(\widehat{c}_{ijf}, X, \alpha, \beta)$ is minimized by zeroing its derivative with respect to X. When we minimize the function $\widehat{\Psi}_X(\widehat{c}_{ijf}, X, \alpha, \beta)$, we cannot obtain its derivative directly because the term $\sum_f \sum_v \|E_v X_f - D_S \alpha_{vf}\|_2^2$ is not separable. Therefore, we

choose the one-step-late method to describe $[E_{\nu}X_f]_l$ as [12]

$$\begin{aligned} &\|E_{\nu}X_{f} - D_{S}\alpha_{\nu f}\|_{2}^{2} = \sum_{l}^{L} \left(\left[E_{\nu}X_{f} \right]_{l} - \left[D_{S}\alpha_{\nu f} \right]_{l} \right)^{2} \\ &\leq \sum_{l}^{L} \sum_{j}^{J} \eta_{\nu,lj} \left(\frac{e_{\nu,lj}}{\eta_{\nu,lj}} \left(x_{jf} - x_{jf}^{k} \right) + \left[E_{\nu}X_{f}^{k} \right]_{l} - \left[D_{S}\alpha_{\nu f} \right]_{l} \right)^{2} \\ &\text{s.t.} \quad \eta_{\nu,lj} = \frac{e_{\nu,lj}}{\sum_{i}^{N} e_{\nu,lj}} \end{aligned}$$

$$(16)$$

where $[E_{\nu}X_f]_l = \sum_j^J \eta_{\nu,lj}([e_{\nu,lj}/\eta_{\nu,lj}](x_{jf} - x_{jf}^k) + [E_{\nu}X_f^k]_l)$ and $[D_S\alpha_{\nu f}]_l$ are the *l*th entries of the vectors $E_{\nu}X_f$ and $D_S\alpha_{\nu f}$, respectively. $e_{\nu,lj}$ is the *lj*th entry of the matrix E_{ν} . Applying the inequality (16) to (15), we arrive at its convex separable surrogate function $\Phi(X; X^k)$

$$\Phi(X; X^k) = \sum_{f}^{F} \sum_{j}^{J} \sum_{i}^{I} \left(g_{ij} x_{jf} - \widehat{c}_{ijf} \log(g_{ij} x_{jf}) \right)
+ p_K (X - D_K \beta)^2 + p_S \sum_{f}^{F} \sum_{v}^{V} \sum_{l}^{L} \sum_{j}^{J} \eta_{v,lj}
\times \left(\frac{e_{v,lj}}{\eta_{v,lj}} \left(x_{jf} - x_{jf}^k \right) + \left[E_v X_f^k \right]_l - \left[D_S \alpha_{vf} \right]_l \right)^2.$$
(17)

We minimize (17) by differentiating with respect to x_{if}

$$\frac{\partial \Phi(X; X^k)}{\partial x_{jf}} = \sum_{i}^{I} g_{ij} - \sum_{i}^{I} \widehat{c}_{ijf} \frac{1}{x_{jf}} + 2p_K (x_{jf} - [D_K \beta]_{jf})
+ 2p_S \sum_{v}^{V} \sum_{l}^{L} e_{v,lj} \left(\frac{e_{v,lj}}{\eta_{v,lj}} (x_{jf} - x_{jf}^k) \right)
+ \left[E_v X_f^k \right]_l - \left[D_S \alpha_{vf} \right]_l$$

$$= 0.$$
(18)

From (18), we find that x_{jf}^{k+1} is the solution of a second-order polynomial equation $Ax_{jf} + B + C(1/x_{jf}) = 0$, where

$$A = 2p_{S} \sum_{v}^{V} \sum_{l}^{L} e_{v,lj} \sum_{j}^{J} e_{v,lj} + 2p_{K}, \quad C = -\sum_{i}^{I} \widehat{c}_{ijf}$$

$$B = 2p_{S} \sum_{v}^{V} \sum_{l}^{L} e_{v,lj} \left(\left[E_{v} X_{f}^{k} \right]_{l} - \left[D_{S} \alpha_{vf} \right]_{l} \right)$$

$$- \left(A_{jf} - 2p_{K} \right) x_{jf}^{k} + \sum_{i}^{I} g_{ij} - 2p_{K} [D_{K} \beta]_{jf}$$
(19)

and where A_{ij} and $[D_K \beta]_{jf}$ are the *ij*th entries of A and $D_K \beta$, respectively.

After several iterations of the E-step and M-step, we can approximately find the true X.

2) α Subproblem: When X and β are fixed, the optimization function of the α subproblem is

$$\min_{\alpha} \sum_{f}^{F} \sum_{v}^{V} \| E_{v} X_{f}^{k} - D_{S} \alpha_{vf} \|_{2}^{2} + \mu_{S} \| \alpha_{vf} \|_{1}. \tag{20}$$

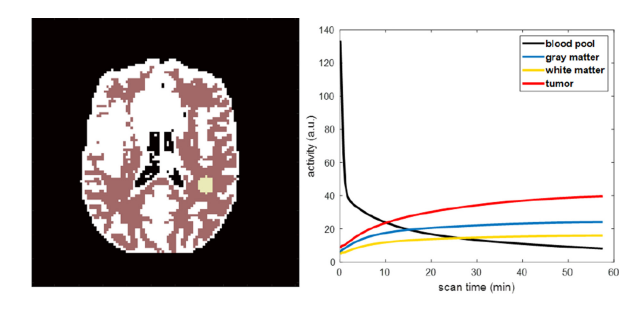


Fig. 3. Structure of the brain phantom (left) and the corresponding TAC curves (right).

It can be solved by the fast-iterative shrinkage thresholding algorithm (FISTA) [42]. FISTA considers minimizing the problem

$$\min f(u) + \lambda g(u). \tag{21}$$

In the α subproblem, $f(\alpha_{vf}) = (1/2) \|E_v X_f^k - D_S \alpha_{vf}\|_2^2$, $g(\alpha_{vf}) = \|\alpha_{vf}\|_1$, and $\lambda = (\mu_S/2)$. The kth iteration of the FISTA algorithm is

$$u^{k} = prox_{t^{k}}(\lambda g) \left(r^{k} - \frac{1}{L} \nabla f(r^{k}) \right)$$

$$t^{k+1} = \frac{1 + \sqrt{1 + 4(t^{k})^{2}}}{2}$$

$$r^{k+1} = u^{k} + \left(\frac{t^{k} - 1}{t^{k+1}} \right) \left(u^{k} - u^{k+1} \right)$$
(22)

where L is a Lipschitz constant. The proximal map is defined by $\operatorname{prox}_{\rho}(\lambda g)(h) = \arg \min_{u} \{\lambda g(u) + (1/2\rho) \|u - h\|^2\}$. Because the proximal map is the same as the soft-thresholding function, the solution of the proximal map can be written as $u = \operatorname{soft}(h, \rho\lambda) = \operatorname{sign}(h) \max\{|h| - \rho\lambda, 0\}$.

3) β Subproblem: When X and α are fixed, the optimization function of the β subproblem is

$$\min_{\beta} \| X^{\top} - D_K \beta \|_{2}^{2} + \mu_K \| \beta \|_{1}. \tag{23}$$

It can also be solved by FISTA [42], where $f(\beta) = (1/2)\|X^{\top} - D_K \beta\|_2^2$, $g(\beta) = \|\beta\|_1$, and $\lambda = (\mu_K/2)$.

III. EXPERIMENTS AND RESULTS

A. Evaluation Criteria

We used brain phantom data and real patient data to evaluate the accuracy of our algorithm. We verified the accuracy of the proposed algorithm by comparing the reconstruction results to the ground truth. To compare the results quantitatively, we used the relative error bias, variance, and MSE. These parameters are defined as follows:

bias =
$$\frac{1}{JF} \sum_{f}^{F} \sum_{i}^{J} \left| x_{jf} - \widehat{x}_{jf} \right| / \widehat{x}_{jf}$$
 (24)

$$var = \frac{1}{F} \frac{1}{J-1} \sum_{f}^{F} \sum_{j}^{J} \left(x_{jf} - \bar{x}_{jf} / \widehat{x}_{jf} \right)^{2}$$
 (25)

$$MSE = \frac{1}{F} \frac{1}{J} \sum_{f}^{F} \sum_{j}^{J} \left\| x_{jf} - \widehat{x}_{jf} \right\|_{2}^{2}.$$
 (26)

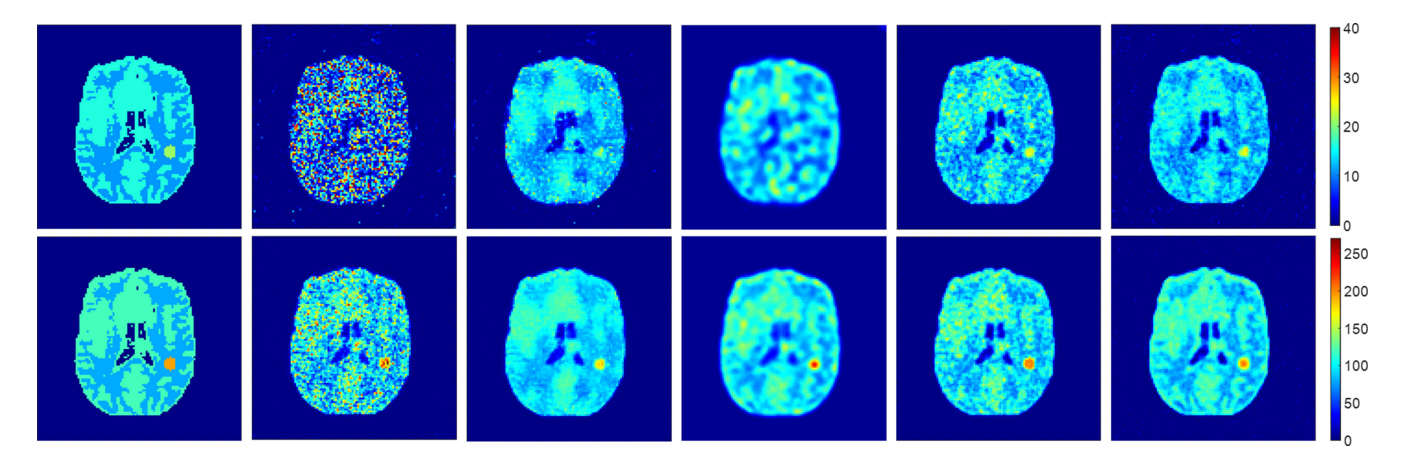


Fig. 4. Left to right: ground truth and the reconstruction results of the MLEM, MLEM+NLM-ST, MLEM+NLM-A, Kernel methods, and DD. First line: the 12th frame; second line: the 22nd frame.

Here, J is the number of pixels in the ROI, whereas x_{if} and \hat{x}_{if} are our reconstruction value and ground truth, respectively, in the jth pixel at the fth frame. \bar{x}_{if} is the mean value of 10 realizations. The bias and variance were averaged over the F frames of the reconstructed images. The bias-variance tradeoff curves were plotted to show the effect of the reconstruction and denoising results. The proposed method (DD) was compared with the classical maximumlikelihood-EM (MLEM) method [41], the dPET images nonlocal means denoising method (NLM-TS) [18], anatomical-prior guided NLM (NLM-A) [43], and PET reconstruction with kernel method [44]. The NLM-TS and NLM-A methods used spatiotemporal image patches and corresponding anatomical image patches for similarity computation, respectively. As for the kernel method, the kernel matrix was generated from composite frames in dPET (Kernel) [44]. In order to evaluate the reconstruction quality of real data, contrast-to-noise ratio is used for quantitative comparison. The CNR is calculated by $CNR = (m_{signal} - m_{background})/std_{background}$, where m_{signal} and $m_{\text{background}}$ are mean value in the corresponding ROIs and std_{background} is the standard deviation of background.

B. Brain Simulation

The brain phantom simulation was performed to evaluate the effect of the proposed method. The computer simulation modeled the Hamamatsu SHE-22000 scanner. The MRI image (T1, 256 \times 256, 1-mm isotropic) was acquired from Brain Web [45]. The PET brain phantom was generated according to the segmented gray matter and white matter in MRI image and a tumor with a diameter of 5 mm was inserted in the white matter. The structure of the PET brain phantom was shown in Fig. 3. The regional TAC curves are shown in the right side of Fig. 3. All the kinetic parameters were followed [46]. The dynamic scan time is 4×20 s, 4×40 s, 4×60 s, 4×180 s, and 8×300 s with total 8 million number of events.

Fig. 4 shows the results using different methods in the 12th frame (up) and 22nd frame (down). Frame 12 has 60-s scan duration and frame 22 has 5-min scan duration. The first column in Fig. 4 is the ground truth. The next five columns are the reconstruction and denoising results of the MLEM,

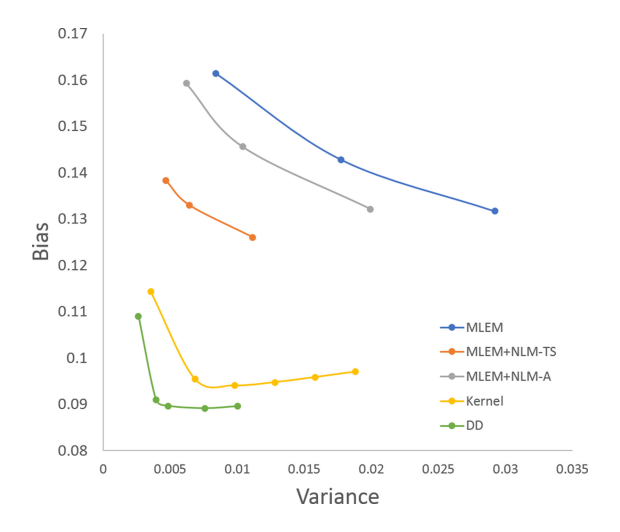


Fig. 5. Tradeoff of bias versus variance for brain phantom using MLEM, MLEM+NLM-TS, MLEM+NLM-A, Kernel, and DD.

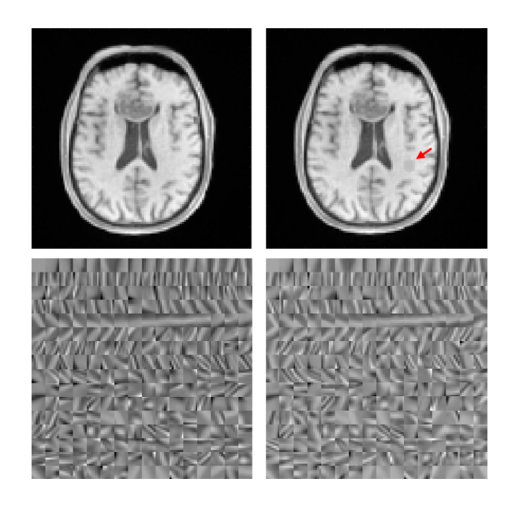


Fig. 6. Left: normal MRI image and its corresponding dictionary for DD; Right: MRI image with hypointense tumor and its corresponding dictionary for DD-T. Pseudo tumor was pointed by red arrow.

MLEM+NLM-TS, MLEM+NLM-A, Kernel, and DD, respectively. For the NLM-ST, the smoothing parameter was set to 0.25. For the MLEM+NLM-A method, the similarity matrix

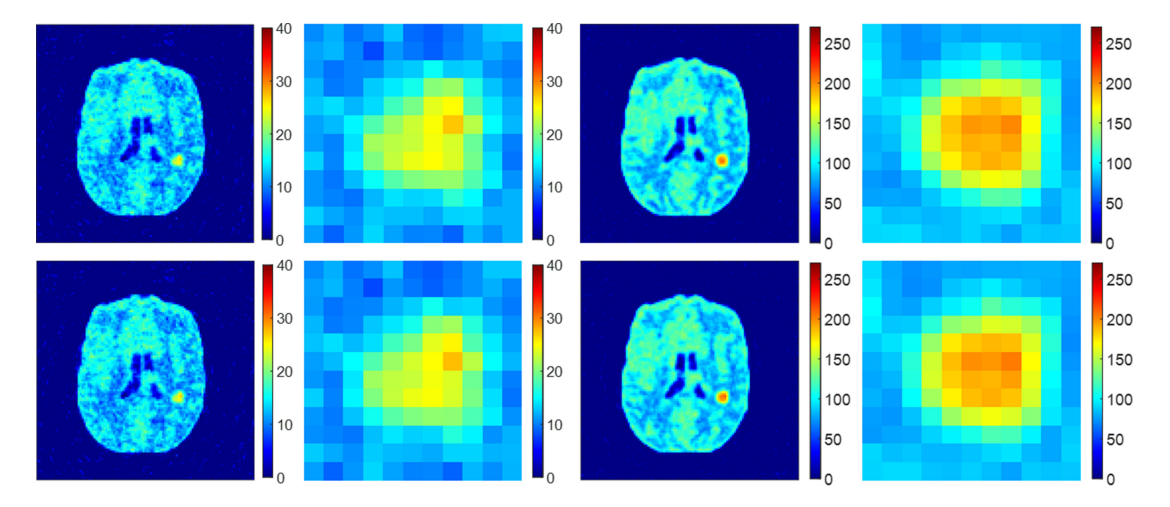


Fig. 7. Reconstruction results for the proposed method using structure dictionary learned from normal MRI image (up) and tumor MRI image (down). Left: 12th frame. Right: 22nd frame.

was generated from the MRI image with a window size of 7×7 and a weighting factor of 1. For the Kernel method, the number of nearest neighbors is 48 and the weighting factor is set to 1. In Fig. 4, the reconstruction images of DD not only maintain a low noise level but also keep clear structure detail in both the 12th and 22nd frames. The NLM-TS results are very smooth, but it is hard to distinguish the boundaries of different structures. Although with the help of anatomical prior from the MRI image, the 12th frame result of MLEM+NLM-A is distorted. This is because MLEM+NLM-A is a static reconstruction method, and its performance was suppressed by the low count number in this frame. In the 22nd frame, the scan duration is longer and MLEM+NLM-A result is much better than the result in the 12th frame. As for the results of the Kernel, the structure was clear, but the noise level is high when compared with DD. The bias versus variance curves are plotted in Fig. 5. It seems when in the same variance level, DD has the lowest bias compared with the other methods.

In order to investigate the impact of the structure dictionary, a hypointense tumor was added to the MRI image at the same location as the PET image, shown in Fig. 6. To avoid a sharp boundary, the tumor was smoothed by a Gaussian filter. The dictionaries learned from normal MRI image and tumor MRI image are shown at the bottom of Fig. 6. Fig. 7 shows the reconstruction results of the proposed method considering situations that tumor is not manifested in the MR image (DD) and tumor is manifested in the MR image (DD-T). The structure dictionary for DD and DD-T is learned from normal MRI image and MRI image with hypointense tumor, which are shown at the bottom of Fig 6. In Fig. 7, DD and DD-T results are nearly the same by visual. The tradeoff bias versus variance curves in tumor ROI for DD and DD-T using different p_s are plotted in Fig. 8. The curves show that DD-T only has a little bit lower bias than DD in the same variance level. It seems that even the lesion is unclear or invisible in the corresponding anatomical image, similar basis from the structure dictionary can represent lesion in PET image.

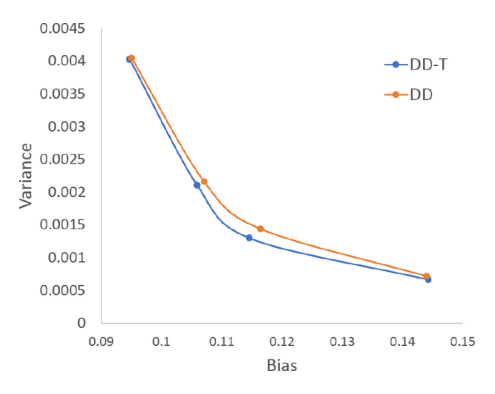


Fig. 8. Tradeoff of bias versus variance for the DD and DD-T.

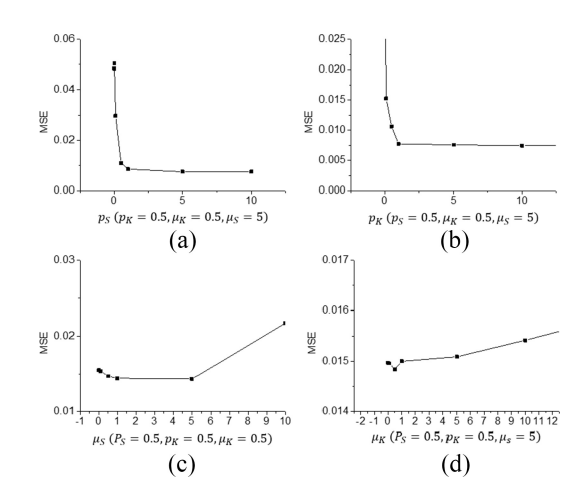


Fig. 9. Dependence of the relative MSE on the different parameters. (a) Structural weighting parameter p_S . (b) Kinetic weighting parameter p_K . (c) Structural sparse parameter μ_{δ} . (d) Kinetic sparse parameter μ_{k} .

C. Implementation Analysis

1) Tuning Parameters: There are four main parameters in our dual-dictionary reconstruction: 1) the structural weighting parameter p_S ; 2) the kinetic weighting parameter p_K ; 3) the structural sparse parameter μ_s ; and 4) the kinetic sparse parameter μ_k . We are going to analyze the impact of these

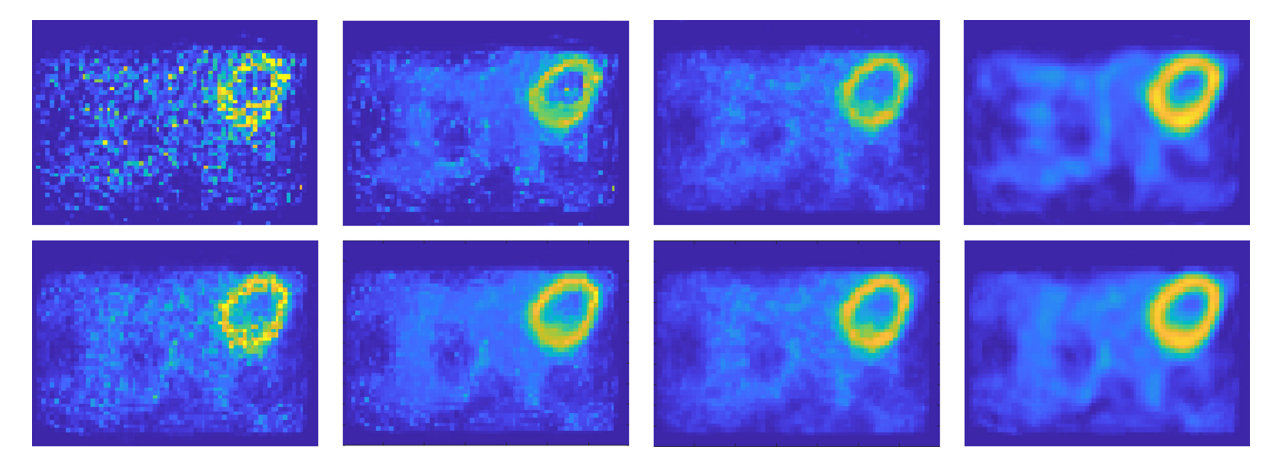


Fig. 10. Reconstruction and denoising result of the real patient data. Left to right: MLEM, MLEM+NLM-ST, Kernel, and DD. Top to bottom: the 4th, and 12th frames.

four parameters on the reconstruction result of the direct simulated data. If we fix $p_K = 0.5$, $\mu_s = 5$, and $\mu_k = 0.5$, and let p_S range from $\{0.01, 0.1, 0.5, 1, 5, 10\}$, the relative MSE is shown in Fig. 9(a). If we fix $p_S = 0.5$, $\mu_s = 5$, and $\mu_k = 0.5$, and let p_K range from 0.01 to 10, the relative MSE is shown in Fig. 9(b). The structural sparse parameter μ_s and the kinetic sparse parameter μ_k are also tuned on the condition that $p_S = 0.5$ and $p_k = 0.5$. The relative MSE of μ_s and μ_k is shown in Fig. 9(c) and (d), respectively. After the tuning, the most suitable parameters can be set as $p_S = 0.5, p_k = 0.5, \mu_s = 5, \text{ and } \mu_k = 0.5.$ The structural weighting parameter p_S and the kinetic weighting parameter p_K control the weight of the structural constraint and kinetic constraint, respectively. If p_S is too small, the effect of the structural constraint has little impact on the result, which leads to a result with high noise. However, if p_S is too large, some boundary details may be lost owing to over smoothing. A relatively large p_K enables the kinetic constraint to preserve the edge efficiently. Both structural sparse parameter μ_s and the kinetic sparse parameter μ_k have good effect when their values are small.

2) Dictionary: In this article, we have proposed a method that exploits a DD to reconstruct a PET image. Therefore, it is important to decide the size of both dictionaries.

The structural dictionary is trained from an anatomical image such as an MR image by using the K-SVD algorithm [37]. According to our experiments, the most suitable size of the structural dictionary was 49×256 with a 7×7 patch size. Choosing a larger patch size may fail to capture fine local structures, whereas choosing a smaller size incurs a longer computational time [24]. Therefore, we chose 7×7 as the most suitable size of the patch.

The compartmental model is used to construct the dictionary of kinetic parameters, which expresses the physical process of nuclide concentration changes over time. When we construct the dictionary, we first need to select a series of coefficients, θ_w . In the experiment, we assumed that the tracer was ¹⁸F-FDG. The decay of the isotope is $\lambda = 0.0001052 \text{ s}^{-1}$. In accordance with the research of Gunn *et al.* [40], we choose

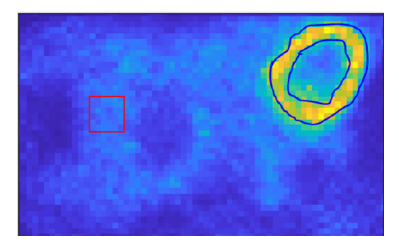


Fig. 11. Background (red) and signal ROIs (blue circle) used to calculate CNR.

 $\theta_{\min} = \lambda$ and let $\theta_{\max} = 0.3 \text{ s}^{-1}$. Then, we set W = 64, which should be large enough to keep the dictionary overcomplete. θ_W is chosen from θ_{\min} to θ_{\max} in a logarithm interval. This produces the kinetic dictionary shown in Fig. 2. This is the input basis of the compartmental model, and several curves spanning the range of W numbers will be chosen in the reconstruction. The real input basis is within the scope of the kinetic dictionary. If W is too small, it cannot cover the real input basis. If W is too large, the spacing of the curves will be small, which is unnecessary.

D. Real Patient Data

A dynamic data set was acquired from a volunteer by the Hamamatsu SHE-22000 whole-body PET scanner with 32 crystal rings. The tracer was ¹⁸F-FDG, and the transaxial resolution of the central field of view was about 3.7 mm/pixel. There were 19 frames in the sinogram, and each of them had 130×96 projections. The size of our reconstructed image was 96×96 . The dynamic scan time is 8×15 s, 2×30 s, 2×120 s, 1×180 s, and 6×300 s. Fig. 10 shows the results for the MLEM, MLEM+NLM-ST, Kernel, and DD methods (left to right) in the 4th and 12th frame (up to down) in parula colormap. Frame 4 has 15-s scan duration and frame 12 has 120-s scan duration. In Fig. 10, DD results show a clear myocardium structure at a low noise level. And the CNRs were calculated to evaluate those reconstruction results. Based on the MLEM reconstruction image, two ROI regions were extracted as signal and background, which is shown in Fig. 11. The CNRs

TABLE I
CNRS FOR MLEM, MLEM+NLM-ST, KERNEL,
AND DD OF REAL PATIENT DATA

| | MLEM | MLEM+NLM-ST | Kernel | DD |
|------------|------|-------------|--------|-------|
| 4th frame | 3.94 | 15.72 | 10.03 | 18.20 |
| 12th frame | 7.18 | 22.17 | 14.16 | 29.48 |

are shown in Table I. The proposed DD method has the highest CNR values among other methods in both 4th and 12th frames.

IV. CONCLUSION

We tested our proposed method on direct simulation data of brain phantom and real patient data. MLEM, MLEM+NLM-ST, MLEM+NLM-A, and Kernel were used for comparison. We found that the proposed DD method was effective for PET image reconstruction. With both structural and kinetic penalties, our method showed a good performance for the direct simulation data and real patient data. The bias versus variance image in Fig. 5 and CNRs of real patient data also demonstrated quantitatively that our method was robust. In the simulation experiment, we also used two MR images, one with lesion and the other without. The results show that the structure dictionary works well even if the lesion is invisible in the anatomical image. In addition, we analyzed the influence that the weighting parameters, the size of the patch, and the number of kinetic dictionaries had on our reconstruction results. The analysis results were useful in enhancing the accuracy of our method.

However, there are some concerns with this reconstruction framework that need to be addressed. There are several parameters in this method. How to choose the parameters need to be carefully considered. Maybe a bilevel learning method can be used to construct a parametrized model to learn parameters by itself. The computing time of our method is obviously longer than that for MLEM. We can possibly use a parallel computing unit, such as a GPU [47] or an FPGA [48] to accelerate our algorithm and make it more practical. A variety of joint imaging patterns, such as PET-CT and PET-MRI that have been recently developed to provide more information on the structure and function for the diagnosis of diseases [49], [50]. Therefore, the DD-based PET imaging reconstruction algorithm can be applied to PET-CT or PET-MR for further analysis. We are planning to carry out further research in this direction. In addition, recent developments on dictionary learning show that it is possible to learn new consecutive tasks based on the previously accumulated experiences [51], [52]. It may be a new direction for us to improve our dictionary designing.

REFERENCES

- [1] K. Ho-Shon, D. Feng, R. A. Hawkins, S. Meikle, M. J. Fulham, and X. Li, "Optimized sampling and parameter estimation for quantification in whole body PET," *IEEE Trans. Biomed. Eng.*, vol. 43, no. 10, pp. 1021–1028, Oct. 1996.
- [2] S. Chen and D. Feng, "Noninvasive quantification of the differential portal and arterial contribution to the liver blood supply from PET measurements using the 11C-acetate kinetic model," *IEEE Trans. Biomed.* Eng., vol. 51, no. 9, pp. 1579–1585, Sep. 2004.

- [3] H. Qiao, J. Bai, Y. Chen, and J. Tian, "Method for tumor recognition with short dynamic PET images: Theory and simulation study," *Progr. Nat. Sci. Mater. Int.*, vol. 19, no. 1, pp. 73–77, 2009.
- [4] A. Bertoldo, P. Vicini, G. Sambuceti, A. A. Lammertsma, O. Parodi, and C. Cobelli, "Evaluation of compartmental and spectral analysis models of ¹⁸F-FFDG kinetics for heart and brain studies with pet," *IEEE Trans. Biomed. Eng.*, vol. 45, no. 12, pp. 1429–1448, Dec. 1998.
- [5] R. Mabrouk, F. Dubeau, and L. Bentabet, "Dynamic cardiac PET imaging: Extraction of time-activity curves using ICA and a generalized Gaussian distribution model," *IEEE Trans. Biomed. Eng.*, vol. 60, no. 1, pp. 63–71, Jan. 2013.
- [6] J. M. M. Anderson, J. R. Votaw, and M. Piccinelli, "Improved PET-based voxel-resolution myocardial blood flow analysis," *IEEE Trans. Rad. Plasma Med. Sci.*, vol. 1, no. 2, pp. 136–146, Mar. 2017.
- [7] M. E. Phelps, "Positron emission tomography provides molecular imaging of biological processes," *Proc. Nat. Acad. Sci. USA*, vol. 97, no. 16, pp. 9226–9233, 2000.
- [8] B. F. Cronin, "The technologist's perspective," in *Positron Emission Tomography*. London, U.K.: Springer, 2006, pp. 27–40.
- [9] S. Chen, H. Liu, Z. Hu, H. Zhang, P. Shi, and Y. Chen, "Simultaneous reconstruction and segmentation of dynamic PET via low-rank and sparse matrix decomposition," *IEEE Trans. Biomed. Eng.*, vol. 62, no. 7, pp. 1784–1795, Jul. 2015.
- [10] S. Tong, A. M. Alessio, P. E. Kinahan, H. Liu, and P. Shi, "A robust state-space kinetics-guided framework for dynamic PET image reconstruction," *Phys. Med. Biol.*, vol. 56, no. 8, pp. 2481–2498, 2011.
- [11] R. M. Leahy and J. Qi, "Statistical approaches in quantitative positron emission tomography," Stat. Comput., vol. 10, no. 2, pp. 147–165, 2000.
- [12] A. R. De Pierro, "On the relation between the ISRA and the EM algorithm for positron emission tomography," *IEEE Trans. Med. Imag.*, vol. 12, no. 2, pp. 328–333, Jun. 1993.
- [13] P. J. Green, "Bayesian reconstructions from emission tomography data using a modified EM algorithm," *IEEE Trans. Med. Imag.*, vol. 9, no. 1, pp. 84–93, Mar. 1990.
- [14] C. A. Bouman and K. Sauer, "A unified approach to statistical tomography using coordinate descent optimization," *IEEE Trans. Image Process.*, vol. 5, no. 3, pp. 480–492, Mar. 1996.
- [15] P. J. Huber, Robust Statistics. Hoboken, NJ, USA: Wiley-Intersci., 2011.
- [16] S. Geman, "Bayesian image analysis: An application to single photon emission tomography," in *Proc. Amer. Stat. Soc. Stat. Comput.*, 1985, pp. 12–18.
- [17] A. Sawatzky, C. Brune, F. Wubbeling, T. Kosters, K. Schafers, and M. Burger, "Accurate EM-TV algorithm in PET with low SNR," in Proc. IEEE Nucl. Sci. Symp. Conf. Rec. (NSS), 2008, pp. 5133–5137.
- [18] J. Dutta, R. M. Leahy, and Q. Li, "Non-local means denoising of dynamic PET images," PLoS ONE, vol. 8, no. 12, 2013, Art. no. e81390.
- [19] T. Merlin, D. Visvikis, P. Fernandez, and F. Lamare, "Dynamic PET image reconstruction integrating temporal regularization associated with respiratory motion correction for applications in oncology," *Phys. Med. Biol.*, vol. 63, no. 4, 2018, Art. no. 045012.
- [20] K. Gong et al., "Iterative PET image reconstruction using convolutional neural network representation," *IEEE Trans. Med. Imag.*, vol. 38, no. 3, pp. 675–685, Mar. 2019.
- [21] J. Xu and H. Liu, "Three-dimensional convolutional neural networks for simultaneous dual-tracer PET imaging," *Phys. Med. Biol.*, vol. 64, no. 18, 2019, Art. no. 185016.
- [22] A. Rahmim et al., "Accurate event-driven motion compensation in high-resolution PET incorporating scattered and random events," *IEEE Trans. Med. Imag.*, vol. 27, no. 8, pp. 1018–1033, Aug. 2008.
- [23] Y. K. Dewaraja, K. F. Koral, and J. A. Fessler, "Regularized reconstruction in quantitative SPECT using CT side information from hybrid imaging," *Phys. Med. Biol.*, vol. 55, no. 9, pp. 2523–2539, 2010.
- [24] S. Chen, H. Liu, P. Shi, and Y. Chen, "Sparse representation and dictionary learning penalized image reconstruction for positron emission tomography," *Phys. Med. Biol.*, vol. 60, no. 2, pp. 807–823, 2015.
- [25] Y. Chen, X. Ye, and F. Huang, "A novel method and fast algorithm for MR image reconstruction with significantly under-sampled data," *Inverse Problems Imag.*, vol. 4, no. 2, pp. 223–240, 2017.
- [26] C. Cobelli, D. Foster, and G. Toffolo, Tracer Kinetics in Biomedical Research: From Data to Model. New York, NY, USA: Springer, 2007.
- [27] E. Carson and C. Cobelli, Modelling Methodology for Physiology and Medicine, 2nd ed. London, U.K.: Elsevier, 2014.
- [28] J.-D. Gallezot, Y. Lu, M. Naganawa, and R. E. Carson, "Parametric imaging with PET and SPECT," *IEEE Trans. Rad. Plasma Med. Sci.*, to be published.

- [29] J. Verhaeghe, D. V. D. Van, I. Khalidov, Y. D'Asseler, I. Lemahieu, and M. Unser, "Dynamic PET reconstruction using wavelet regularization with adapted basis functions," *IEEE Trans. Med. Imag.*, vol. 27, no. 7, pp. 943–959, Jul. 2008.
- [30] S. Tong and P. Shi, "Tracer kinetics guided dynamic PET reconstruction," *Inf. Process. Med. Imag.*, vol. 20, no. 20, pp. 421–433, 2007.
- [31] J. Tang, H. Kuwabara, D. F. Wong, and A. Rahmim, "Direct 4D reconstruction of parametric images incorporating anato-functional joint entropy," *Phys. Med. Biol.*, vol. 55, no. 15, pp. 4261–4272, 2010.
- [32] P. Novosad and A. J. Reader, "MR-guided dynamic PET reconstruction with the kernel method and spectral temporal basis functions," *Phys. Med. Biol.*, vol. 61, no. 12, pp. 4624–4644, 2016.
- [33] K. Gong, J. Cheng-Liao, G. Wang, K. T. Chen, C. Catana, and J. Qi, "Direct Patlak reconstruction from dynamic PET data using kernel method with MRI information based on structural similarity," *IEEE Trans. Med. Imag.*, vol. 37, no. 4, pp. 955–965, Apr. 2018.
- [34] D. J. Kadrmas and G. T. Gullberg, "4D maximum a posteriori reconstruction in dynamic SPECT using a compartmental model-based prior," *Phys. Med. Biol.*, vol. 46, no. 5, pp. 1553–1574, 2001.
- [35] J. Yan, B. Planeta-Wilson, and R. E. Carson, "Direct 4D list mode parametric reconstruction for PET with a novel EM algorithm," in *Proc. IEEE Nucl. Sci. Symp. Conf. Rec.*, 2008, pp. 3625–3628.
- [36] J. Cui, K. Gong, N. Guo, K. Kim, H. Liu, and Q. Li, "CT-guided PET parametric image reconstruction using deep neural network without prior training data," in *Medical Imaging 2019: Physics of Medical Imaging*, vol. 10948, T. G. Schmidt, G.-H. Chen, and H. Bosmans, Eds., Int. Soc. Opt. Photon., 2019, pp. 238–243.
- [37] M. Aharon, M. Elad, and A. Bruckstein, "K-SVD: An algorithm for designing overcomplete dictionaries for sparse representation," *IEEE Trans. Signal Process.*, vol. 54, no. 11, pp. 4311–4322, Nov. 2006.
- [38] R. N. Gunn, S. R. Gunn, and V. J. Cunningham, "Positron emission tomography compartmental models," J. Cereb. Blood Flow Metab. vol. 21, no. 6, pp. 635–652, 2001.
- [39] J. Cui, H. Yu, S. Chen, Y. Chen, and H. Liu, "Simultaneous estimation and segmentation from projection data in dynamic PET," *Med. Phys.*, vol. 46, no. 3, pp. 1245–1259, 2019.
- [40] R. N. Gunn, S. R. Gunn, F. E. Turkheimer, J. A. Aston, and V. J. Cunningham, "Positron emission tomography compartmental models: A basis pursuit strategy for kinetic modeling," *J. Cerebr. Blood Flow Metab.*, vol. 22, no. 12, pp. 1425–1439, 2002.

- [41] L. A. Shepp and Y. Vardi, "Maximum likelihood reconstruction for emission tomography," *IEEE Trans. Med. Imag.*, vol. MI-1, no. 2, pp. 113–122, Oct. 1982.
- [42] A. Beck and M. Teboulle, "A fast iterative shrinkage-thresholding algorithm for linear inverse problems," SIAM J. Imag. Sci., vol. 2, no. 1, pp. 183–202, 2009.
- [43] C. Chan, S. Meikle, R. Fulton, G.-J. Tian, W. Cai, and D. D. Feng, "A non-local post-filtering algorithm for PET incorporating anatomical knowledge," in *Proc. IEEE Nucl. Sci. Symp. Conf. Rec. (NSS/MIC)*, 2009, pp. 2728–2732.
- [44] G. Wang and J. Qi, "PET image reconstruction using kernel method," *IEEE Trans. Med. Imag.*, vol. 34, no. 1, pp. 61–71, Jan. 2015.
- [45] C. A. Cocosco, V. Kollokian, R. K.-S. Kwan, G. B. Pike, and A. C. Evans, "Brainweb: Online interface to a 3D MRI simulated brain database," *NeuroImage*, vol. 5, p. 425, 1997.
- [46] D. D. Feng, K.-P. Wong, C.-M. Wu, and W.-C. Siu, "A technique for extracting physiological parameters and the required input function simultaneously from PET image measurements: Theory and simulation study," *IEEE Trans. Inf. Technol. Biomed.*, vol. 1, no. 4, pp. 243–254, Dec. 1997.
- [47] J. L. Herraiz, S. España, J. Cal-González, J. J. Vaquero, M. Desco, and J. M. Udías, "Fully 3D GPU PET reconstruction," *Nucl. Inst. Methods Phys. Res. A*, vol. 648, no. 3, pp. S169–S171, 2011.
- [48] M. Haselman, R. Miyaoka, T. K. Lewellen, and S. Hauck, "FPGA-based data acquisition system for a positron emission tomography (PET) scanner," in *Proc. Int. ACM/SIGDA Symp. Field Program. Gate Arrays*, 2008, p. 264.
- [49] E. S. K. See, "A new novel PET/CT reconstruction algorithm by using prior image model with simulated annealing process," in *Proc. Int. Symp. Intell. Signal Process. Commun. Syst.*, 2005, pp. 661–664.
- [50] M. J. Ehrhardt et al., "Joint reconstruction of PET-MRI by exploiting structural similarity," *Inverse Problems*, vol. 31, no. 1, 2014, Art. no. 015001.
- [51] G. Sun, Y. Cong, and X. Xu, "Active lifelong learning wit 'watchdog," in *Proc. 32nd AAAI Conf. Artif. Intell.*, 2018, pp. 4107–4114.
- [52] G. Sun, C. Yang, J. Liu, L. Liu, X. Xu, and H. Yu, "Lifelong metric learning," *IEEE Trans. Cybern.*, vol. 49, no. 8, pp. 3168–3179, Aug. 2019.